

Angular Dispersion and Anomalous Transmission Cast Ultramonochromatic X Rays

Yuri Shvyd'ko, Stanislav Stoupin, Deming Shu, and Ruben Khachatryan
Advanced Photon Source, Argonne National Laboratory, Argonne, Illinois 60439, USA
 (Dated: October 23, 2018)

Optical spectrometers, instruments that work with monochromatic light, are commonly rated by the spectral bandwidth, which defines the ability to resolve closely spaced spectral components. The ability to detect faint objects among these components, spectral contrast, is another desired aspect. Here we demonstrate that a combined effect of angular dispersion (AD) and anomalous transmission (AT) of x rays in Bragg reflection from asymmetrically cut crystals can shape spectral distributions of x rays to profiles with record high contrast and small bandwidths.

The AD&AT x-ray optics is implemented as a five-reflection three-crystal arrangement featuring a combination of the above mentioned attributes, so much desirable for x-ray monochromators and analyzers: a spectral contrast of $\simeq 500$, a bandwidth of $\simeq 0.46$ meV and a remarkably large angular acceptance of $\simeq 107$ μ rad. The new optics can become a foundation for the next generation inelastic x-ray scattering spectrometers for studies of atomic dynamics.

PACS numbers: 41.50.+h, 42.25.-p, 61.05.cp, 07.85.Nc

NOTATIONS

Notations and their definitions are listed below in order of appearance. They are similar to those used in [1].

E	Photon energy.
E_0	Average or peak photon energy.
ΔE	Spectral bandwidth.
$\Delta E_H^{(s)}$	Intrinsic spectral width in symmetric Bragg diffraction.
ΔE_M	Bandwidth of the monochromator spectral resolution function (FWHM).
η, η_H	Asymmetry angle - angle between reflecting atomic planes and crystal face.
θ, θ_H	Glancing angle of incidence.
θ', θ'_H	Glancing angle of reflection.
Ψ	Offset between the angle of anomalous transmission and Bragg reflection peaks.
Θ	Angle of incidence $\Theta = \pi/2 - \theta$.
E_R	Center energy of the region of exact Bragg back-reflection.
Θ_R	Center incidence angle of the region of exact Bragg back-reflection.
d_H	spacing between the reflecting atomic planes.
h	Planck's constant.
c	Speed of light in vacuum.
$f_M(E)$	Monochromator spectral resolution function.
C_M	Contrast of the spectral resolution function.
ΔE_C	Energy offset at which spectral contrast is measured.
\mathbf{H}	Diffraction vectors: $\mathbf{H} = \mathbf{C}, \mathbf{D}_1, \mathbf{F}, \mathbf{D}_2$, or \mathbf{W} .
\mathbf{C}	Collimator.
\mathbf{D}	Dispersing element.
\mathbf{F}	Anomalous transmission filter.
\mathbf{W}	Wavelength selector.
(hkl)	Miller indices of the diffraction vector \mathbf{H} .
b_H	Asymmetry parameter.
$\Delta\theta_H^{(s)}$	Intrinsic angular width in symmetric diffraction.
$w_H^{(s)}$	Refraction correction in symmetric diffraction.
d	Crystal thickness.
λ	X-ray wavelength.

λ_R	Center wavelength of the region of exact Bragg back-reflection.
$\Delta\theta_M$	Angular acceptance of the monochromator.
$\Delta\theta'_M$	Angular divergence of x rays emanating from the monochromator.
$\Delta\theta_H$	Angular width of a generic Bragg reflection.
$\Delta\theta'_H$	Angular width of reflected x rays for a generic Bragg reflection.
$\tilde{\Theta}_D$	Rotation angle of D-crystals.
$\Delta E_{M \otimes A}$	Bandwidth of the combined spectral resolution functions of the monochromator and analyzer.
$\Delta E_{1/10000}$	Spectral half width at the 10^{-4} level fraction of the maximum.
ε_M	Average spectral efficiency of the monochromator.
I_0	Incident photon flux.
I_M	Photon flux transmitted through the monochromator.
ΔE_0	Bandwidth of the spectral distribution of the incident radiation.
θ_M	Rotation angle of the monochromator.
θ_A	Rotation angle of the analyzer.

INTRODUCTION

Despite many recent advances in inelastic x-ray and neutron scattering critical voids exist in current experimental capabilities for investigation of atomic dynamics in biomaterials (DNA, lipid bilayers, proteins), in many intriguing classes of oxide materials (high temperature superconductors, colossal magnetoresistance manganites, multiferroics), and many other materials with diverse properties of fundamental and practical interest. This void calls for new hard x-ray spectrometers capable of not only achieving small spectral bandwidths ΔE in the 0.1-1 meV range ($\Delta E/E \approx 10^{-7} - 10^{-8}$), but, more importantly, the ability to detect faint spectral objects, which requires small bandwidth at the $10^{-3} - 10^{-4}$ level fraction of the spectral resolution function maximum. In

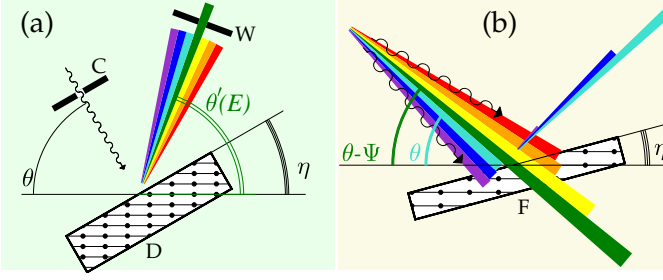


FIG. 1: Basic phenomena underlying the AD&AT x-ray optics. In x-ray Bragg diffraction from atomic planes composing nonzero angle η to the crystal entrance face, the crystal acts (a) like an optical prism dispersing the photons into a divergent x-ray fan with photons of different energies E propagating at different reflection angles $\theta'(E)$ - effect of angular dispersion (AD) [1, 10–12], (b) as a filter with anomalously high transparency for x rays with incidence angles $\theta - \Psi$ in the immediate vicinity ($\Psi \approx 5 \mu\text{rad}$) but smaller than the Bragg angle θ - effect of anomalous transmission (AT) [13–15].

this paper, we present a new concept for achieving highly monochromatic x rays with steeply declining tails (large spectral contrast) as well as its realization.

Principles of monochromatization of hard x rays in essence are based on Bragg diffraction of x rays from periodic gratings of atomic planes in single crystals (for review and references see, e.g., [1]). Spectral band in which x rays are reflected, the Bragg diffraction intrinsic width $\Delta E_H^{(s)}$, is typically small, not more than $\Delta E_H^{(s)}/E_0 \simeq 10^{-4}$ if measured relative to an average photon energy E_0 . The smallness of $\Delta E_H^{(s)}$ is determined first of all by a macroscopically large number of reflecting atomic planes, as well as by crystal and atomic properties. The intrinsic Bragg bandwidth can be reduced [2–9] by using the so-called asymmetric x-ray diffraction, diffraction from atomic planes at nonzero angle η to the crystal face - Fig. 1. Still, the bandwidth cannot be tailored to arbitrary small values without significant loss in Bragg reflectivity.

The intrinsic Bragg reflection width $\Delta E_H^{(s)}$ basically sets the limit for the smallest band in which x rays can be selected with a given Bragg reflection, and, therefore, sets the limit for monochromatization of x rays. This fundamental limitation, can be overcome if an effect of angular dispersion in Bragg diffraction from asymmetrically cut crystals [1, 10, 11] is used, as proposed in [1]. Bragg diffraction of x rays from asymmetrically cut crystals have the same effect on x rays as an optical prism on visible light: an incident collimated x-ray beam is fanned-out upon reflection with photons of different energies propagating at different angles $\theta'(E)$ - Fig. 1(a), with a dispersion rate

$$\frac{d\theta'}{dE} = \frac{2}{E} \frac{\sin \theta \sin \eta}{\sin(\theta - \eta)} \xrightarrow{\theta \rightarrow 90^\circ} \frac{2 \tan \eta}{E}, \quad (1)$$

as demonstrated in [12]. By picking out photons in a small angular range $\Delta\theta'$ from the fan, the bandwidth ΔE_M of the selected x rays can be reduced to any small value, independent of how large is the intrinsic Bragg reflection width $\Delta E_H^{(s)}$. In the proof of the principle experiments [12, 16] it was confirmed that the angular dispersion indeed can be used to overcome the Bragg reflection width limitation, though, no spectacular small bandwidths has been achieved until now. In this paper we introduce an advanced x-ray optics with enhanced angular dispersion, allowing to monochromatize x rays to bandwidths $\Delta E_M/\Delta E_H^{(s)} \simeq 10^{-2}$, which is almost two orders of magnitude smaller than the relative intrinsic bandwidth of the applied Bragg reflection.

However, achieving steep tails of the spectral function, i.e., high spectral contrast[28], is the most challenging task in monochromatization of x rays. Steep tails are equally important in spectroscopic applications. Dynamical theory of x-ray Bragg diffraction in crystals predicts that the tails of the spectral reflection function decline slowly $\propto 1/(E - E_0)^2$, for a single Bragg reflection. While suppression of the tails can be achieved using a sequence of Bragg reflections, a more dramatic improvement is demonstrated here. Tails as steep as those of the Gaussian distribution can be obtained with a qualitatively new approach based on the effect of anomalous transmission of x rays in Bragg diffraction from asymmetrically cut crystals [13–15]. In fact, it is a combination of angular dispersion and anomalous transmission which yields the extremely steep tails and a narrow bandwidth. The effect of angular dispersion due to an asymmetric Bragg reflection is illustrated in Fig. 1(a). The combined effect is illustrated in Fig. 1(b). A part of the dispersion fan with glancing angles of incidence $\theta - \Psi$ in the immediate vicinity ($\Psi \approx 5 \mu\text{rad}$) but smaller than the Bragg angle θ propagates through the crystal with anomalously low absorption, while the rest of the dispersion fan is abruptly rejected by the Bragg reflection.

A novel x-ray optics introduced here is based on the phenomena of angular dispersion and anomalous transmission. Particularly, we describe the underlying principles, design and performance of a three-crystal five-reflection monochromator, featuring a combination of superlative properties, such as, exceptionally steep tails of the spectral profile, an extremely narrow bandpass, an extraordinary large angular acceptance, high efficiency, and the in-line configuration (i.e., the incident and the resulting monochromatic x rays are parallel and propagate in the same direction). The small bandpass is due to angular dispersion [1, 10–12] and the steep tails are due to anomalous transmission [13–15].

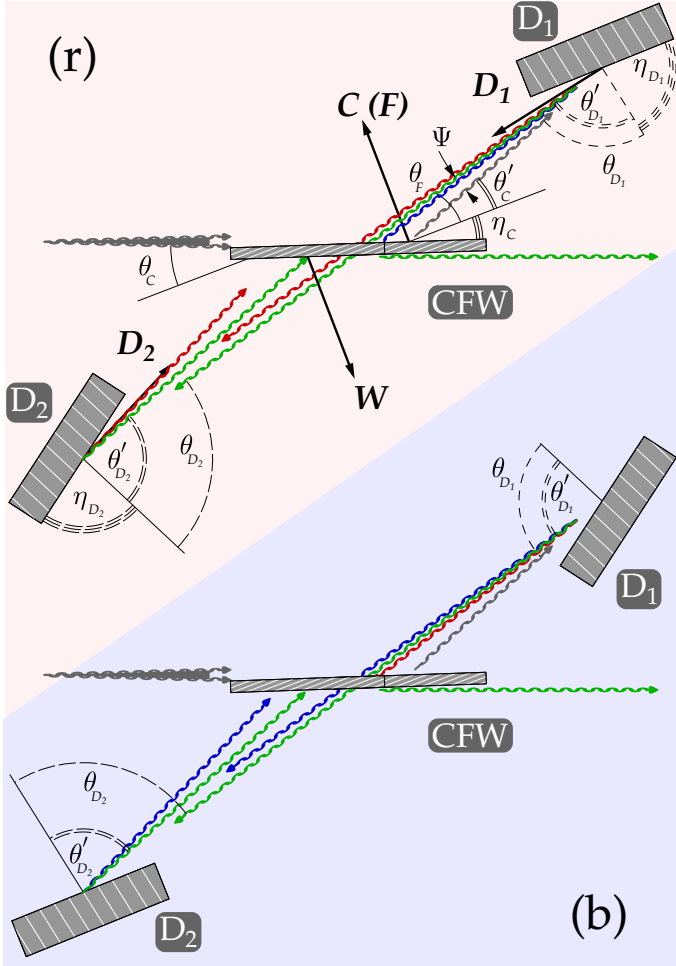


FIG. 2: Optical scheme of the in-line three-crystal five-reflection CDFDW monochromators (r) red-winged and (b) blue-winged, respectively. The CFW crystal, executes three key functions, a collimator -C, an anomalous transmission filter -F, and a wavelength selector -W in successive reflections. The crystals D_1 and D_2 are dispersing elements. All crystals are asymmetrically cut with the reflecting atomic planes shown by the white lines, perpendicular to the diffraction vectors \mathbf{H} ($\mathbf{H} = \mathbf{C}, \mathbf{F}, \mathbf{D}_1, \mathbf{D}_2$, or \mathbf{W}), composing non-zero asymmetry angle η_H to the entrance surface. θ_H and θ'_H are the glancing angles of incidence and reflection, respectively.

AD&AT OPTICS PRINCIPLES AND IMPLEMENTATION

X-ray monochromators which employ the effect of angular dispersion, require three fundamental optical elements, each performing a distinct key function, as schematically shown in Fig. 1(a). First, a collimator (C-element) accepts x rays with a large angular spread and collimates into a beam with a small angular divergence. Secondly, a dispersing element (D-element) spreads the collimated beam by means of an asymmetric Bragg reflection into a fan with different spectral components propagating at different angles. Thirdly, a wavelength selector

(W-element) selects photons from the fan in a small angular, and, therefore, spectral range [1]. An angular dispersive monochromator with each of the three elements represented by an individual crystal, a CDW monochromator, have been demonstrated in [16].

Here we introduce novel x-ray optics with a combined effect of angular dispersion (AD) and anomalous transmission (AT) to produce x rays with a spectral distribution having both very steep tails and small bandwidths. The AD&AT optics contains an additional element, the anomalous transmission filter (F-element). The AD&AT optics is realized here by three crystals executing five successive reflections with key functions C, D, F, D, and W respectively (the scheme was first proposed by Yu. Shvyd'ko in [17]). Therefore, in the following it is termed as CDFDW monochromator. The four key functions C,D,W, and F, are performed by three crystals: CFW, D_1 , and D_2 , in two symmetric but nonequivalent configurations: termed hereafter red-winged - Fig. 2(r), and blue-winged - Fig. 2(b)[29].

The CFW-crystal is a thin asymmetrically cut crystal combining C-, F-, and W-functions. Incident x rays with a wide angular divergence are collimated to a beam with a small divergence upon the first asymmetric Bragg reflection at glancing angle of reflection θ'_C from the CFW-crystal. The collimated beam impinges then on the dispersing element D_1 at a glancing angle of incidence θ_{D_1} in almost exact backscattering $\theta'_{D_1} - \theta_{D_1} = \Psi$. The asymmetry angle η_{D_1} is chosen close to 90° . The proximity to exact backscattering and $\eta_{D_1} \Rightarrow 90^\circ$ are important, first, to ensure the largest effect of angular dispersion (1) and, secondly, to minimize blurring of the angular dispersion contrast, which may arise due to the angular spread of x rays incident onto the D-crystal [1]. The collimated incident x-ray beam is fanned-out upon reflection from D_1 with photons of different energies propagating towards the CFW crystal at different glancing angles of reflection $\theta'_{D_1}(E)$. The CFW crystal now acts as the F-element. Transmission of photons which impinge upon the crystal at an angle $\theta_F = \theta'_C - \Psi$ is anomalously enhanced. This angle of anomalous transmission is smaller than the Bragg reflection angle by $\Psi \approx 5 \mu\text{rad}$ (cf. Fig. 1). In the next step, x rays are reflected from crystal D_2 in the same fashion as from D_1 . The resulting angular dispersion rate is that of the single reflection (Eq. (1)) increased by a factor of two, i.e.

$$\frac{d\theta'_{D_2}}{dE} = \frac{4 \tan \eta_{D_2}}{E}. \quad (2)$$

In the final, fifth reflection, the CFW crystal in the W-function selects x rays in a small angular, and, therefore, spectral range [30].

Those photons are preferentially transmitted through the monochromator, whose energy E and angle of incidence θ_D to D-crystals are related by the condition of exact backscattering (a small angular offset $\Psi/2$ is ne-

crystal/ function	\mathbf{H}	η_H	θ_H	b_H	$\Delta E_H^{(s)}$	$\Delta\theta_H^{(s)}$	$w_H^{(s)}$	d
	(hkl)	[deg]	[deg]		[meV]	[μ rad]	$\times 10^{-6}$	[mm]
CFW/C	(2 2 0)	19.0	20.7	-0.047	565	23.5	47.2	0.3
D ₁ /D	(8 0 0)	88.0	89.9	-1	27	1870	9.13	20
CFW/F	($\bar{2}$ $\bar{2}$ 0)	19.0	20.7	-21.5	565	23.5	47.2	0.3
D ₂ /D	(8 0 0)	88.0	89.9	-1	27	1870	9.13	20
CFW/W	(2 2 0)	19.0	20.7	-21.5	565	23.5	47.2	0.3

TABLE I: Elements of the CDFDW optics, and their crystal, and Bragg reflection parameters as used in all presented here dynamical theory calculations and in the experiment: (hkl) - Miller indices of the Bragg diffraction vector \mathbf{H} , η_H - asymmetry angle, θ_H - glancings angle of incidence, $b_H = -\sin(\theta_H \pm \eta_H)/\sin(\theta_H \mp \eta_H)$ - asymmetry parameter, d - crystal thickness, $\Delta E_H^{(s)}$, $\Delta\theta_H^{(s)}$, and $w_H^{(s)}$ - are Bragg's reflection intrinsic spectral width, angular acceptance, and refraction correction in symmetric scattering geometry, respectively. X-ray photon energy $E = 9.1315$ keV.

glected), because only such photons are also transmitted through the CFW-crystal. Due to angular dispersion, exact backreflection from an asymmetrically cut crystal takes place, unlike symmetric diffraction case, for each photon energy E at different angular deviation $\Theta = \pi/2 - \theta$ from normal incidence to the reflecting atomic plane, as shown in [1, 12]. The relation between the angle of incidence Θ and photon energy E for exact backscattering is given by

$$\Theta - \Theta_R = \frac{E - E_R}{E_R} \tan \eta_H,$$

$$\Theta_R = w_H^{(s)} \tan \eta_H, \quad E_R = \frac{hc}{2d_H} (1 + w_H^{(s)}). \quad (3)$$

with Θ_R as the angle of incidence and E_R as the photon energy in the center of the Bragg reflection region, $w_H^{(s)}$ is Bragg's reflection refraction correction, and d_H is distance between the reflecting atomic planes associated with the reciprocal vector \mathbf{H} . This relation suggest that by changing simultaneously the angles of incidence to D-crystals, the energy tuning of the CDFDW monochromator can be achieved. An angular variation of $\delta\Theta_D$ according to Eq. (3) results in a photon energy variation

$$\delta E = E_R \frac{\delta\Theta_D}{\tan \eta_D}. \quad (4)$$

The presented above qualitative picture is supported by calculation of the spectral distributions of x rays after each successive reflection, based on the dynamical theory of x-ray diffraction in crystals. The distributions are shown in Figs. 3(r) and (b). Crystal parameters used in the calculations are given in Table I. The divergence of the incident beam was assumed to be $20 \mu\text{rad}$. The spectral distribution upon the 1st Bragg reflection from the CFW-crystal is very broad in agreement with large

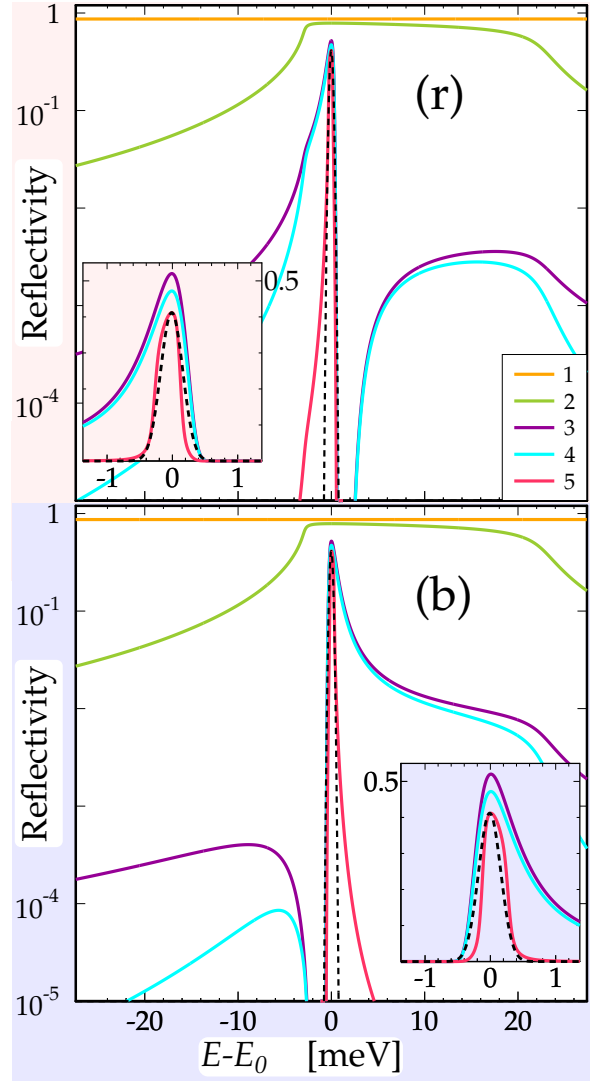


FIG. 3: Dynamical theory calculations of the spectral distribution of x rays after each successive reflection (indicated by number and color) from the crystals of the CDFDW optics in the red-winged - Fig. 2(r), and in the blue-winged configuration - Fig. 2(b), respectively. Black dashed lines show Gaussian distribution of the same full width at half maximum. Insets show the distributions on the linear scale.

spectral width of the (220) Bragg reflection. After the 2nd reflection, the bandwidth is reduced to the intrinsic width $\Delta E_H^{(s)} = 27$ meV of the (800) Bragg reflection from crystal D₁. A dramatic change in the spectral distribution occurs in anomalous transmission through the CFW-crystal, in the 3rd interaction. In the 4th reflection, from crystal D₂, the spectral distribution practically does not change, as its Bragg reflection bandwidth is already much broader than the incident spectral width. The main function of D₂ is to increase the angular dispersion rate by a factor of two, i.e., the opening of the angular dispersion fan - Eq. (2). In the 5th reflection, the CFW-crystal selects x rays in a small angular range, and therefore re-

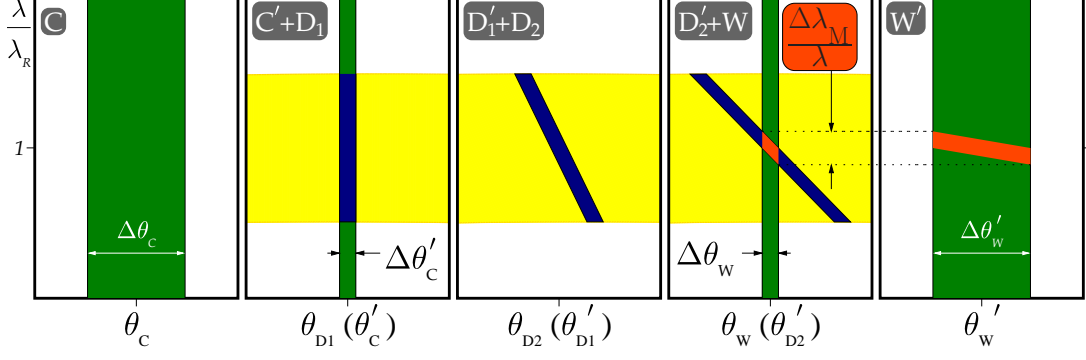


FIG. 4: DuMond diagrams for a sequence of four asymmetric Bragg reflections from crystals functioning as C-, D₁-, D₂-, or W-element. Anomalous transmission in the F-element is not taken into account. Green and yellow stripes are the regions of Bragg reflections in the space of x-ray wavelengths λ and angles of incidence θ_H or reflection θ'_H from an H-element (H=C, D₁, D₂, or W). Blue stripes display the overlapping reflection regions of the C- and D-elements. Orange tetragons display the reflection region common for all elements. D-element is set into backscattering ($\theta_D \rightarrow \pi/2$) with the center of the reflection spectral range at $\lambda_R = hc/E_R$ - Eq. (3).

duces further the bandwidth to $\Delta E_M = 0.4$ meV. The peak throughput is 40 %.

The evolution of the spectral distributions shows that the most dramatic change happens in the 3rd step, when in anomalous transmission the CFW-crystal cuts abruptly the angular dispersion fan from one side, and reduces it from another. The thicker the crystal, the steeper the tail is. It is very close or even steeper than the slope of the Gaussian function shown by black dashed line in Figs. 3(r) and (b). The effect of anomalous dispersion resulting in the extremely steep tail on one side is so large, that the wavelength selector in the 5th reflection improves the spectral distribution only on the opposite side. Thus, anomalous transmission is essential for the formation of both small bandwidth and the steep tails.

The tail can be as steep as that of the Gaussian function, however, only on one side. For the blue-winged crystal configuration shown in Fig. 2(b) the steep tail is on the low-energy side, while in the other red-winged configuration in Fig. 2(r), it is on the high-energy side. Apparently, one can think of an AD&AT optics in CDF_rF_bDW or simply CDF_rF_b configuration, with two F-elements, which would produce the steep tails on both sides. These options will be studied elsewhere.

DuMond diagram analysis [18] provides a valuable graphical presentation and insight into the complex machinery of the multi-reflection optics. The relative spectral bandwidth $\Delta E_M/E$, the angular acceptance $\Delta\theta_M$ of the monochromator, and the angular divergence $\Delta\theta'_M$ of x rays emanating from the monochromator can be ex-

pressed to a good accuracy in simple terms by

$$\frac{\Delta E_M}{E} = \frac{\Delta\lambda_M}{\lambda} = \frac{\Delta\theta'_C + \Delta\theta_W}{4 \tan \eta_D}, \quad (5)$$

$$\Delta\theta_M = \Delta\theta_C^{(s)} / \sqrt{|b_C|}, \quad (6)$$

$$\Delta\theta'_M = \Delta\theta_W^{(s)} \sqrt{|b_W|}. \quad (7)$$

They are derived using DuMond diagrams in Fig. 4, in the way similar to how they were derived for the CDW-monochromator in [1]. The assignment of reflection regions is given in the Figure caption. We note that the inclination of the reflection region (blue stripe in panel D₂'-W) representing wavelength-angular distribution of x rays reflected from the D₂-element is two times greater than the inclination of the reflection region, which represents the distribution of x rays upon reflection from the D₁-element (blue stripe in panel D₁'-D₂). As a result, the bandwidth ΔE_M (Eq. (5)) is a factor of two smaller than the bandwidth of the CDW monochromator with the same crystal parameters. Equation (5) demonstrates an important distinguishing feature of the angular dispersive monochromators: the spectral bandwidth ΔE_M is independent of the intrinsic spectral width of the Bragg backreflection of the D-crystal. It depends on the strength of the effect of angular dispersion, expressed by $\tan \eta_D$, and it depends on the geometrical parameters, such as the angular spread $\Delta\theta'_C = \Delta\theta_C^{(s)} \sqrt{|b_C|}$ of the photons emanating from the collimator crystal C and incident on the dispersing element, and, on the angular acceptance $\Delta\theta_W = \Delta\theta_W^{(s)} / \sqrt{|b_W|}$ of the wavelength selector W. Another distinguishing feature, the angular acceptance of the CDFDW optics is determined solely by the angular acceptance of the C-element - Eq. (6), and it can be made large, more than 100 μrad , by choosing low indexed Bragg reflections.

	ΔE_M	$\Delta E_{M \otimes A}$	$\Delta E_{1/10000}$	C_M	$\Delta \theta_M$	ε_M
	[meV]	[meV]	[meV]		[μ rad]	%
Theory	0.4	0.56	1.0	1000	105	22
Experiment	0.46	0.65	3.2	500	107	16

TABLE II: Design and measured parameters of the CDFDW monochromator: ΔE_M - full width at half maximum (FWHM) of the spectral resolution function of a single monochromator; $\Delta E_{M \otimes A}$ - FWHM for a combined spectral resolution functions of the blue-winged monochromator and the red-winged analyzer; $\Delta E_{1/10000}$ - spectral half width at the 10^{-4} level fraction of the maximum on the side of the spectral resolution function with steeper tail, C_M - spectral contrast, $\Delta \theta_M$ angular acceptance, and ε_M average spectral efficiency. The latter is defined as $\varepsilon_M = I_M/I_0 \times \Delta E_0/\Delta E_M$, with I_0 as incident and I_M transmitted through the monochromator photon flux, and ΔE_0 as FWHM of the incident radiation spectral distribution.

DEMONSTRATION OF THE AD&AT OPTICS

Two CDFDW monochromators, one in blue- and the other in red-winged configuration, have been designed, built, and commissioned at the Advanced Photon Source (APS), 30-ID beamline, to study key questions, whether the AD&AT optics is capable in practice to mold the spectral distribution of x rays to profiles with steeply declining tails, small bandwidths, and can be applied to x-ray beams with large angular divergence. Parameters of the crystals used in the monochromators are given in Table I. Design monochromator parameters are given in Table II. Technical details on the experimental set-up, monochromator's mechanical design, crystal fabrication and characterization, crystal alignment procedure, crystal temperature control, and other experimental details will be provided in additional publications [19, 20].

Perfect implementation of the angular dispersion and anomalous transmission effects is critical for achieving the anticipated performance of the AD&AT optics. Measurements presented in Fig. 5, and discussed in the following, demonstrate that both effects perform close to theoretical expectations. The studies are performed in the CDF configuration as shown schematically by the scattering diagrams in the insets of Figure 5. The beam is collimated to $\simeq 1 \mu$ rad divergence after the first reflection from the CFW-crystal, monochromatized to $\simeq 27$ meV bandwidth upon backreflection from the D_1 -crystal, then transmitted through the CFW- crystal, and recorded using a photon counting detector (Det.) as a function of $\tilde{\Theta}_{D_1}$, the angular coordinate of the D_1 -crystal. The variation of the rotation angle $\delta \tilde{\Theta}_{D_1}$ directly relates to the variation of the incidence angle to CFW by $\delta \theta_F = 2\delta \tilde{\Theta}_{D_1}$.

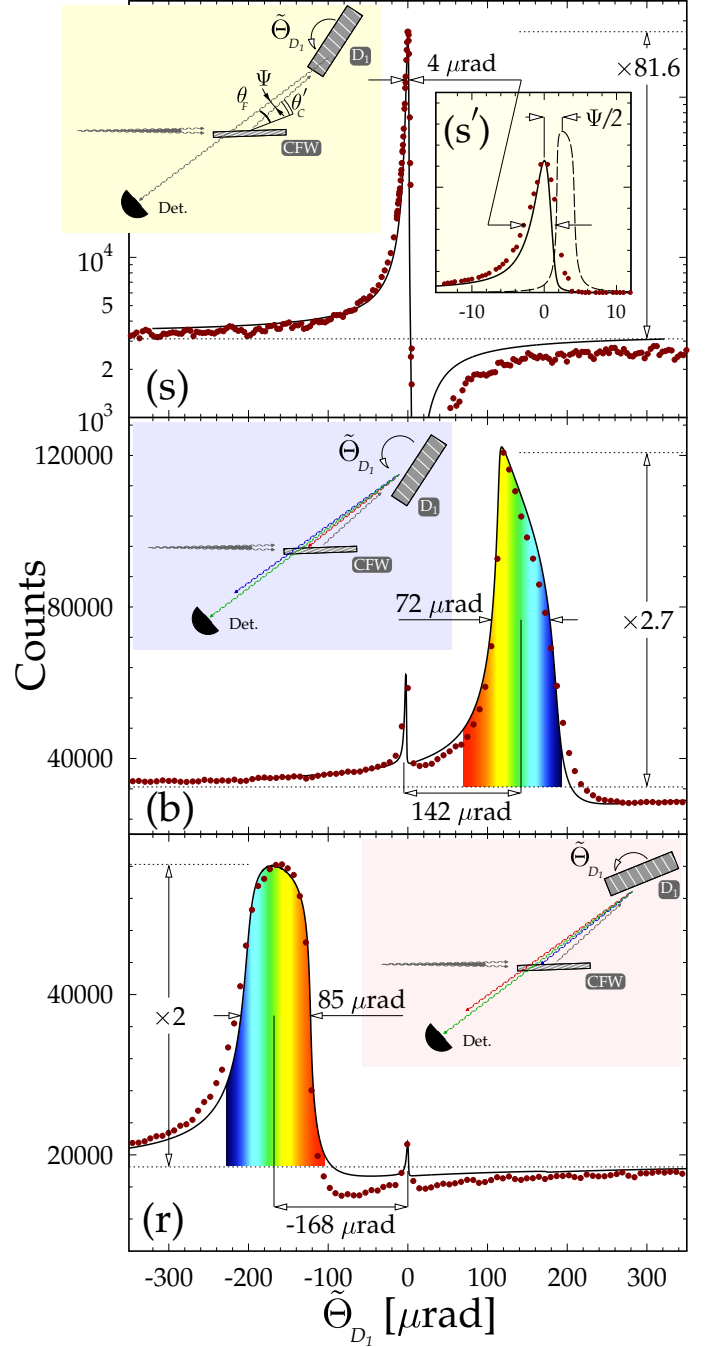


FIG. 5: Angular distributions of x-ray intensity upon a sequence of interactions $C \rightarrow D_1 \rightarrow F$, schematically shown in the insets, representing: (s) effect of anomalous transmission, and (b), (r) combined effect of angular dispersion and anomalous transmission of x rays in Bragg diffraction from asymmetrically cut crystals. Sharp line ($\simeq 4 \mu$ rad) in (s) is due to backreflection and subsequent anomalous transmission taking place for all photon energies at the same incidence angle to crystal D_1 (same rotation angle $\tilde{\Theta}_{D_1} = 0$). In contrast, in (b) and (r) backreflection takes place at different angles for different photon energies, indicated by color. Solid and dashed lines are dynamical theory calculations, and solid circles are experimental data. (s') shows same dependences as (s) but on the linear scale.

Anomalous Transmission

Results presented in Figs. 5(s) and (s') are obtained when the lateral face of the D_1 crystal is illuminated. For simplicity, we refer to this configuration as *symmetric*, since the reflecting atomic planes compose small asymmetry angle with the lateral face. The recorded intensity (Counts) is shown by solid circles in Figs. 5(s) on the logarithmic scale. A sharp asymmetric transmission peak is observed with the position of the maximum chosen at $\tilde{\Theta}_{D_1} = 0$. The peak value exceeds by a factor of $\gtrsim 80$ the normal level of transmission, indicated by the lower horizontal dotted line. This is an enhancement of the anomalous transmission effect an order of magnitude greater than the largest previously reported in literature [15]. The experimental curve is overall in a good agreement with the theoretical dependence shown by the solid black line, though the angular width of $4 \mu\text{rad}$ is somewhat broader than $2.5 \mu\text{rad}$ expected in theory. It has a typical for the angular dependence of anomalous transmission dispersion form with a very steep edge changing over into a broad minimum on the positive $\tilde{\Theta}_{D_1}$ side.

Figure 5(s') shows the same two dependences on the linear scale. In addition, the dashed line represents a calculated angular dependence of the accompanying Bragg reflection from the CFW crystal which was not measured in the experiment. It shows that, the reflection peak is shifted by only $\tilde{\Theta}_{D_1} = \Psi/2$ ($\Psi = 5 \mu\text{rad}$) with respect to the transmission peak. Thus, in agreement with expectations, the CFW crystal transmits x rays only at an angle of incidence $\theta_F = \theta'_C - \Psi$, which differs from the glancing angle of reflection θ'_C . In other words, the CFW crystal transmits x rays which are only in almost exact backreflection from D_1 crystal. The experimental facts demonstrate that the effect of anomalous transmission is perfectly working.

Angular Dispersion and Anomalous Transmission

Figures 5(r) and (b) show results of similar measurements, however, with the x-ray beam reflected from the asymmetrically cut face of the D_1 crystal, in the red- and blue-winged configurations, respectively. Unlike the previous case, the anomalous transmission takes place in a much broader $\simeq 72 - 85 \mu\text{rad}$ angular range of the rotation angle $\tilde{\Theta}_{D_1}$, and the maximum is observed at $\tilde{\Theta}_{D_1} \simeq 142 \mu\text{rad}$ (b) and at $\tilde{\Theta}_{D_1} \simeq -168 \mu\text{rad}$ (r), respectively. (The weak sharp peaks are of the same nature and at the same angular position $\tilde{\Theta}_{D_1} = 0$ as the peak in Fig. 5(s), appearing because a small part of the incident beam still illuminates the lateral crystal face of the D_1 crystal.) Nothing has changed, compared to the previous case, with the condition for anomalous transmission through the CFW crystal: it takes place only at an an-

gle of incidence $\theta_F = \theta'_C - \Psi$. What has dramatically changed is the backreflection condition, by transition to diffraction from the asymmetrically cut crystal face.

Now, in asymmetric diffraction - Figs. 5(b) and (r), backreflection from D_1 takes place, in agreement with Eq. (3), at different angles for different photon energies as indicated by the color, i.e., in a broad angular range, which peak is also shifted by Θ_R . Using Eq. (3) and the crystal parameters from Table I, we obtain $\Theta_R \simeq 168 \mu\text{rad}$. The angular width of the exact Bragg backscattering from crystal D_1 with intrinsic spectral width $\Delta E_{D_1}^{(s)} = 27 \text{ meV}$, can be estimated using Eq. (3) as $\Delta\Theta = (\Delta E_{D_1}^{(s)}/E_R) \tan \eta_{D_1} \simeq 85 \mu\text{rad}$. The measured values shown in Fig. 5(b) agree well, while values shown in Fig. 5(r) perfectly, with these estimations. The interplay between anomalous transmission and angular dispersion, which is not taken into account in this estimation, is different in the two cases, resulting in different shapes, positions, widths, and amplitudes of the peaks. Rigorous multi-crystal dynamical theory x-ray diffraction calculations shown by solid lines are in good agreement in both cases, with regard to the width, position, amplitude of anomalous transmission, and shape of the exact backscattering peak. These observations demonstrate an overall good functioning of both effects of angular dispersion and anomalous transmission.

CDFDW Angular Acceptance

The two CDFDW monochromators were aligned, one in blue-, another in red-winged configuration - Figs. 6-8 [31]. Their performance was evaluated in terms of angular acceptance, widths and contrast of the spectral function, and the average spectral efficiency. Measured values as well as design parameters are given in Table II. The values are obtained from the appropriate angular and spectral dependences shown in Figs. 6, 7, and 8, respectively, along with the schemes of the experimental arrangements.

The angular acceptance has been measured by rotation of a CDFDW monochromator, and by counting photons arriving at its exit after the five reflections. Blue circles in Fig. 6 represent the measured dependence, while the solid line represent the results of the multi-crystal dynamical theory calculations for the incident beam with a $\simeq 15 \mu\text{rad}$ divergence, and a $\Delta E_0 = 0.6 \text{ eV}$ bandwidth, as in the experiment. There is a very good correspondence between the measured and calculated dependences, with an angular acceptance of $\Delta\theta_M = 107 \mu\text{rad}$. This is an unusually large number. Typically, the angular acceptance of high-resolution x-ray monochromators is in a 10 to $20 \mu\text{rad}$ range, often requiring collimating optics, such that the x rays from the source to be fully accepted by the monochromator [2, 4-9, 21]. The only exception to

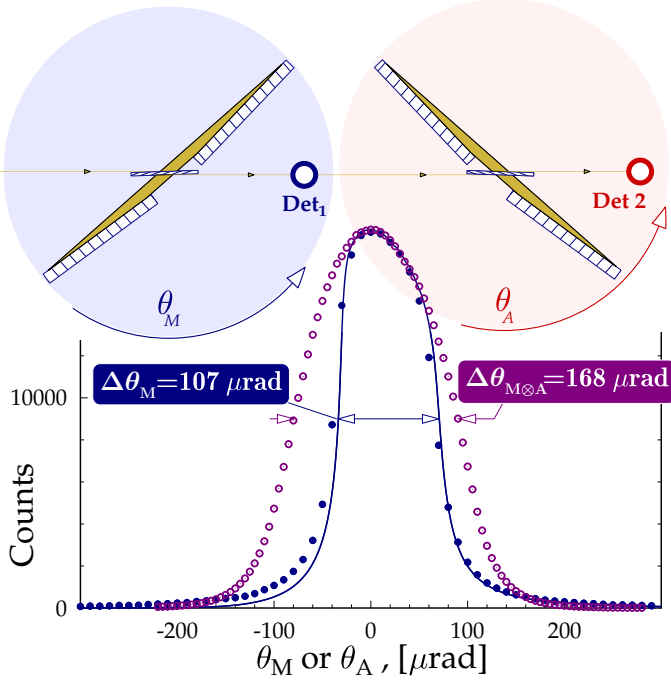


FIG. 6: Experimental scheme and angular dependence of transmission through CDFDW monochromators. Solid blue circles show results for the blue-winged monochromator with incident beam collimated to $\simeq 15 \mu\text{rad}$, as measured by Det₁ x-ray detector. Solid line - theory. Open purple circles: show results for the red winged analyzer with the incident beam emanating from the monochromator, set to the transmission maximum, as measured by Det₂ x-ray detector.

this rule are single bounce monochromators [22], which, however, have a disadvantage of long Lorentzian tails in the spectral resolution function.

In the second measurement presented by the purple open circles, the beam from the first monochromator (set to the transmission maximum) is guided through the second monochromator, which is rotated about its axis. The width of the angular dependence in this measurement is $\simeq 168 \mu\text{rad}$, about 50% broader than the angular width measured with the direct beam. This agrees with the expectation that the angular divergence of x rays from the CDFDW monochromator $\Delta\theta'_M$ has to be as large as the angular acceptance $\Delta\theta_M$ - Eqs. (6)-(7), and therefore the broader angular curve is a result of the convolution of a $\simeq 100 \mu\text{rad}$ divergent beam with $\simeq 107 \mu\text{rad}$ angular acceptance of the monochromator.

CDFDW Spectral Resolution Function

The peak photon energy of the monochromator spectral resolution function can be tuned by changing simultaneously the angles of incidence θ_{D_1} and θ_{D_2} (Fig. 2), as formally expressed by Eq. (3). This can be accomplished

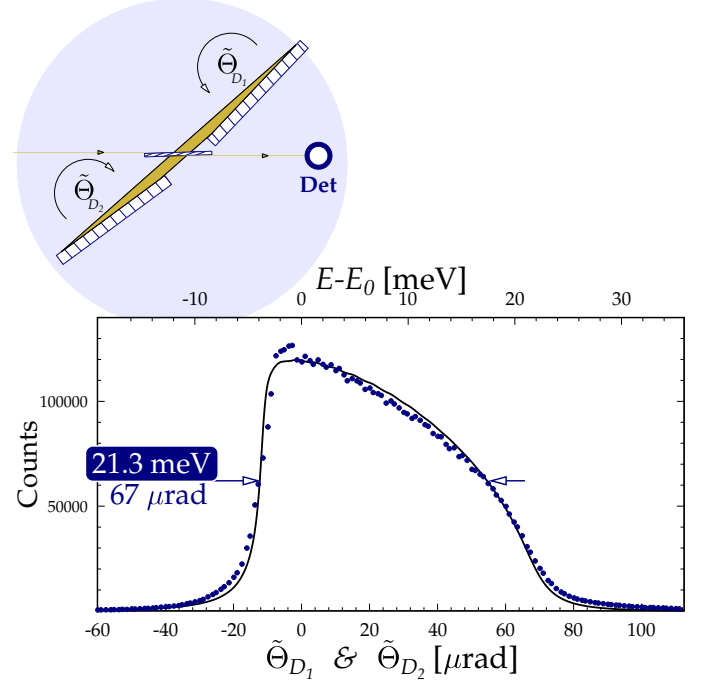


FIG. 7: Experimental scheme and a spectral tuning curve of the CDFDW monochromator measured by rotation of the D-crystals. The blue circles show experimental data, while the solid line - calculations using multi-crystal dynamical theory of x-ray diffraction.

through simultaneous rotation of the D-crystals with rotation angles $\tilde{\theta}_{D_1}$ and $\tilde{\theta}_{D_2}$, as shown in the scheme of Fig. 7. The relationship between the angular and energy variations in our case $\delta E/\delta\tilde{\theta}_D = 0.319 \text{ meV}/\mu\text{rad}$, which is obtained from Eq. (4), and crystal parameters in Table I.

Solid dots in Fig. 7 represent thus measured spectral tuning curve of the CDFDW monochromator. The solid line shows the results of the theoretical calculations, which is in a good agreement with the experimental data. The width of the tuning curve is related to the intrinsic width $\Delta E_D^{(s)} = 27 \text{ meV}$ of the D-crystal reflection curve. The measured tuning curve width ($\simeq 21 \text{ meV}$) is, however, smaller, because it represents the width of the product of two Bragg reflection curves resulting from the sequence of two backreflections. The tuning curve shows that the available tuning range is relatively small, if the energy is changed by rotation of D-crystals. The tuning range can be increased by varying the temperature of D-crystals [16], which would result in the change of the lattice parameter d_H and backscattering energy E_R - Eq. (3).

The CDFDW monochromator spectral resolution function was measured by changing the monochromator energy (by rotation of D-crystals), and using another monochromator as an analyzer, as shown in the scheme of Fig. 8. Convolution of the spectral resolution func-

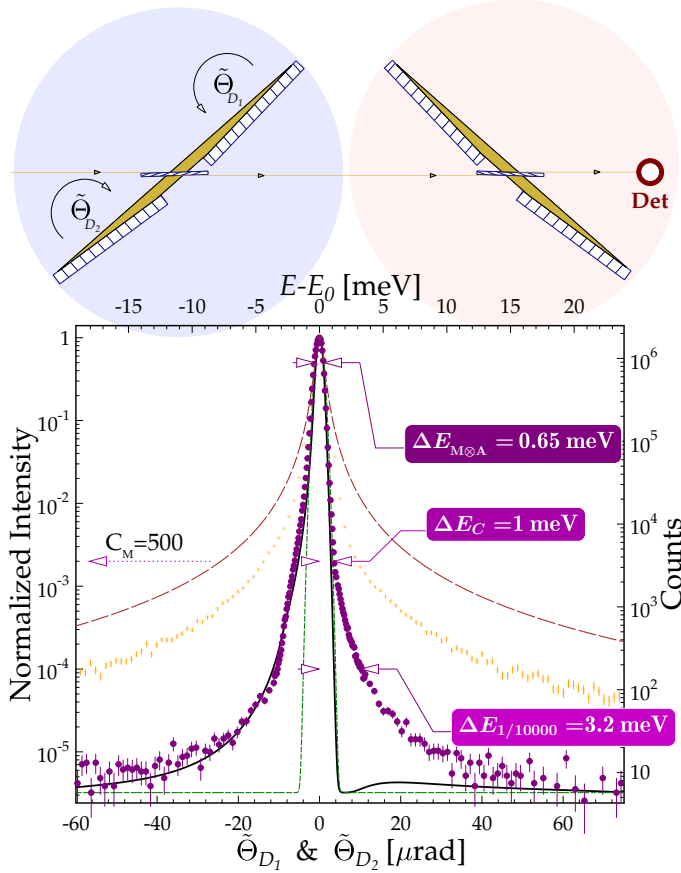


FIG. 8: Experimental scheme and combined spectral resolution function of the blue-winged CDFDW monochromator measured against the red-winged analyzer. The purple circles show experimental spectral resolution function, the black solid line - spectral functions calculated using multi-crystal dynamical theory of x-ray diffraction. Other functions with the same FWHM are shown for comparison: green dashed line - Gaussian; dark-red dashed line - Lorentzian, orange open circles - experimental dependence for a four-crystal monochromator [23].

tions of the monochromator and the analyzer, a combined spectral resolution function, is measured in this case. The expected CDFDW spectral function is asymmetric with the very steep tail on one side - Figs. 3(r) and (b). For the combined spectral resolution function to preserve the steep tail, the monochromator and analyzer have to be chosen, such that one is in the blue- and the other in the red-winged configuration. The steep tail of the combined spectral resolution function will be reproduced on the side where the spectral function of the device which is not tuned has the steep tail. In our experiment, the blue-winged monochromator is tuned, and the red-winged analyzer is at a fixed energy.

The purple solid circles in Fig. 8 show the results of the measurements of the combined spectral resolution function on the logarithmic scale. An x-ray detector is in-

stalled downstream the analyzer. The full width at half maximum is $\Delta E_{M\otimes A} = 0.65$ meV, which is close to the design value of 0.56 meV. It is important to note, that this very high resolution is achieved with an x-ray beam incident upon the analyzer, that has a large angular divergence of $\Delta\theta'_M \simeq 100$ μ rad. Most importantly, the function has a steeply declining tails especially on the high-energy side with spectral contrast $C_M \simeq 500$, and a half width at the 10^{-4} level fractions of the maximum $\Delta E_{1/10000} = 3.2$ meV. Theory predicts even steeper tail, shown by the black solid line in Fig. 8 with $C_M \simeq 10^3$, and $\Delta E_{1/10000} = 1.0$ meV. The discrepancy is attributed to yet not fully perfect sub-surface layer of silicon crystals used in the experiment. Improvements in crystal fabrication are in progress [20]. Nonetheless, we are measuring a spectral function with remarkably steep tails. First, the experimental curve follows the tails of the Gaussian function over almost three orders of magnitude. Secondly, the measured curve is more than an order of magnitude steeper than the tails of the best spectral resolution functions measured with the state-of-the-art multi-crystal x-ray optics. The orange circles show an example of such resolution function for a four-crystal monochromator designed for nuclear resonant scattering experiments with 14.4 keV photons [23]. It has been measured using a very well collimated ($\simeq 3$ μ rad) incident x-ray beam, and a $\simeq 50$ -neV-broad nuclear resonance as an analyzer. Thirdly, the tails of the combined CDFDW spectral resolution function is two orders of magnitude steeper than the tails of the Lorentzian distribution with the same FWHM. It should be noted that the long Lorentzian tails (spectral contrast $C_M = 11$), are typical for spectral resolution functions of all existing inelastic x-ray scattering (IXS) spectrometers [24–27]. For the Lorentzian tails to reach the level of the measured CDFDW resolution function, the width of the Lorentzian distribution would have to be reduced to 65 μ eV. The latter has to be compared with a 1.5 meV width (a more than 20 times larger value) of the spectral resolution functions presently available with the state-of-the-art IXS spectrometers.

The last but not least, the measured average spectral efficiency $\varepsilon_M = 16$ %, is close to 22 % expected in theory (see Table II caption for the definition of ε_M).

In conclusion, the angular dispersive and anomalously transmissive x-ray (AD&AT) optics offer a possibility to shape x-ray spectra to distributions with steeply declining tails (large contrast), and small bandwidth. The AD&AT optics is applicable to x rays with a large spread of angles of incidence. Introduced here, a three-crystal, five-reflection AD&AT x-ray optics, the CDFDW monochromators feature a combination of superlative properties: exceptionally steep tails of the spectral profile, extremely narrow bandpass, extraordinary large angular acceptance, high efficiency, and in-line configuration. The monochromators and analyzers based on this principles have a potential to become key optical compo-

nents in the next generation ultra-high resolution inelastic x-ray scattering spectrometers, and other applications in x-ray science.

ACKNOWLEDGMENTS

We are grateful to Linda Young for supporting this project in its decisive phase at the APS. We are indebted to J.-H. Kim (APS), X. Huang (APS), and J. Sutter (DLS), for help with the experiments at the APS 30-ID beamline. T. Roberts (APS) is acknowledged for long standing technical support, K. Goetze (APS) for developing monochromator controls, M. Wiczorek for help with crystal fabrication, L. Assoufid, Q. Qian, and J. Mai with metrology, K. Mundboth (DLS) for help with developing temperature control. A.I. Chumakov (ESRF) is acknowledged for providing unpublished data. S.P. Collins (DLS), C. Burns (WMU), Y. Cai (BNL), S.-H. Chen (MIT), J.P. Hill (BNL), B.C. Larson (ORNL), G. Monaco (ESRF), D. Reznik (Uni. of Colorado at Boulder), G. Ruocco (Sapienza University of Rome), Q. Shen (BNL), and T. Rayment (DLS) are acknowledged for stimulating interest and valuable suggestions. Work was supported by the U.S. Department of Energy, Office of Science, Office of Basic Energy Sciences, under Contract No. DE-AC02-06CH11357.

-
- [1] Yu. Shvyd'ko, *X-Ray Optics – High-Energy-Resolution Applications*, vol. 98 of *Optical Sciences* (Springer, Berlin Heidelberg New York, 2004).
 - [2] A. I. Chumakov, J. Metge, A. Q. R. Baron, H. Grünsteudel, R. Rüffer, and T. Ishikawa, *Nucl. Instrum. Methods Phys. Res. A* **383**, 642 (1996).
 - [3] T. S. Toellner, M. Y. Hu, W. Sturhahn, K. Quast, and E. E. Alp, *Appl. Phys. Lett.* **71**, 2112 (1997).
 - [4] T. S. Toellner, *Hyp. Interact.* **125**, 3 (2000).
 - [5] A. I. Chumakov, R. Rüffer, O. Leupold, A. Barla, H. Thiess, T. Asthalter, B. Doyle, A. Snigirev, and A. Q. R. Baron, *Appl. Phys. Lett.* **77**, 31 (2000).
 - [6] M. Yabashi, K. Tamasaku, S. Kikuta, and T. Ishikawa, *Rev. Sci. Instrum.* **72**, 4080 (2001).
 - [7] T. S. Toellner, M. Hu, W. Sturhahn, G. Bortel, E. E. Alp, and J. Zhao, *J. Synchrotron Rad.* **8**, 1082 (2001).
 - [8] T. S. Toellner, A. Alatas, A. Said, D. Shu, W. Sturhahn, and J. Zhao, *Journal of Synchrotron Radiation* **13**, 211 (2006).
 - [9] T. S. Toellner, A. Alatas, and A. H. Said, *Journal of Synchrotron Radiation* **18**, 605 (2011).
 - [10] M. Kuriyama and W. J. Boettinger, *Acta Cryst.* **A32**, 511 (1976).
 - [11] S. Brauer, G. Stephenson, and M. Sutton, *J. Synchrotron Rad.* **2**, 163 (1995).
 - [12] Yu. V. Shvyd'ko, M. Lerche, U. Kuetgens, H. D. Rüter, A. Alatas, and J. Zhao, *Phys. Rev. Lett.* **97**, 235502 (2006).
 - [13] H. Wagner, *Z. f. Physik* **146**, 127 (1956).
 - [14] S. Kishino, *J. Phys. Soc. Jpn.* **31**, 1168 (1971).
 - [15] R. Bubáková, M. Hrivnáková, and Z. Šourek, *Czechoslovak Journal of Physics* **25**, 1321 (1975).
 - [16] Yu. V. Shvyd'ko, U. Kuetgens, H. D. Rüter, M. Lerche, A. Alatas, and J. Zhao, *AIP Conf. Proc.* **879**, 737 (2007).
 - [17] Yu. Shvyd'ko, in *NSLS-II, Conceptual Design Report* (Brookhaven National Laboratory, December, 2006), chap. 11.5.2 Conceptual Design for the Inelastic X-Ray Scattering Beamline, pp. 11–39 – 11–45, <http://www.bnl.gov/nsls2/project/CDR>.
 - [18] J. W. M. DuMond, *Phys. Rev.* **52**, 872 (1937).
 - [19] D. Shu, S. Stoupin, R. Khachatryan, K. Goetze, T. Roberts, and Yu. V. Shvyd'ko (Symposium on SPIE Optical Engineering and Applications, San Diego, California, USA, 2011), submitted.
 - [20] S. Stoupin, Yu. V. Shvyd'ko, R. Khachatryan, D. Shu, and et al, (2001) to be published.
 - [21] A. Q. R. Baron, Y. Tanaka, D. Ishikawa, D. Miwa, M. Yabashi, and T. Ishikawa, *J. Synchrotron Rad.* **8**, 1127 (2001).
 - [22] R. Verbeni, F. Sette, M. Krisch, U. Bergmann, B. Gorges, C. Halcoussis, K. Martel, C. Masciovecchio, J. F. Ribois, G. Ruocco, et al., *J. Synchrotron Rad.* **3**, 62 (1996).
 - [23] A. Chumakov (2011), CRL \otimes 2 Si(440) \otimes 2 Si(1222) monochromator for 14.4 keV X-rays, private communication.
 - [24] C. Masciovecchio, U. Bergmann, M. Krisch, G. Ruocco, F. Sette, and R. Verbeni, *Nucl. Instrum. Methods Phys. Res. B* **117**, 339 (1996).
 - [25] A. Q. R. Baron, Y. Tanaka, D. Miwa, D. Ishikawa, T. Mochizuki, K. Takeshita, S. Goto, T. Matsushita, H. Kimura, F. Yamamoto, et al., *Nucl. Instrum. Methods Phys. Res. A* **467-468**, 627 (2001).
 - [26] H. Sinn, *J. Phys.: Condensed Matter* **13**, 7525 (2001).
 - [27] A. H. Said, H. Sinn, and R. Divan, *Journal of Synchrotron Radiation* **18**, 492 (2011).
 - [28] The contrast of the spectral resolution function $f_M(E)$, is defined as a ratio $C_M = f(0)/f(\Delta E_C)$ of the peak intensity to the intensity of the tail at an offset $E = \Delta E_C = 1.578 \Delta E_M$. Here ΔE_M is the bandwidth of $f_M(E)$. The spectral contrast is thus a dynamic range available to resolve a faint feature with an energy resolution equal to ΔE_C . The offset ΔE_C is chosen such that the contrast of the Gaussian function $C_M = 10^3$. For the Lorentzian function it is two orders of magnitude smaller: $C_M = 11$.
 - [29] Anomalous transmission was embedded in the original proposal of the CDW scheme [1], therefore in the present terminology it should be defined as CDFW. However the CDFDW scheme is more advantageous mostly due to doubled dispersion rate, and in-line geometry
 - [30] The coplanar scattering geometries shown in Fig. 2, are not mandatory. Wave-vectors of x rays reflected from CFW- and D-crystals may have components perpendicular to the scattering plane in the presented scheme. Non-coplanar scattering geometry adds a possibility of tuning the photon energy in broader range and mitigate the adverse effect of multiple reflections in exact backscattering from D-crystals [20]. However, this may compromise the spectral resolution, as discussed in [1]
 - [31] The red-winged CDFDW optics shown in the schemes of Fig. 2(r) and Figs. 6, 8 are equivalent. In the experiments we realized the scheme shown in Figs. 6, 8 as it offered better possibilities for strain-free crystal mount [20].